Tailored grain morphology via a unique melting strategy in electron beam-powder bed fusion

Downloaded from: https://research.chalmers.se, 2022-01-01 18:26 UTC

Citation for the original published paper (version of record):
Karimi, P., Sadeghi, E., Ålgårdh, J. et al (2021)
Tailored grain morphology via a unique melting strategy in electron beam-powder bed fusion
Materials Science & Engineering A: Structural Materials: Properties, Microstructure and Processing, 824
http://dx.doi.org/10.1016/j.msea.2021.141820

N.B. When citing this work, cite the original published paper.

research.chalmers.se offers the possibility of retrieving research publications produced at Chalmers University of Technology.
It covers all kind of research output: articles, dissertations, conference papers, reports etc. since 2004.
research.chalmers.se is administrated and maintained by Chalmers Library

(article starts on next page)

Materials Science & Engineering A 824 (2021) 141820

Contents lists available at ScienceDirect

Materials Science & Engineering A

journal homepage: www.elsevier.com/locate/msea

Tailored grain morphology via a unique melting strategy in electron beam-powder bed fusion

Paria Karimi [a,*], Esmaeil Sadeghi [a], Joakim Ålgårdh [b], Jonas Olsson [a], Magnus Hörnqvist Colliander [c], Peter Harlin [d], Ehsan Toyserkani [e], Joel Andersson [a]

[a] Department of Engineering Science, University West, 461 86, Trollhättan, Sweden
[b] Arcam-EBM (a GE Additive), 435 33, Mölnlycke, Sweden
[c] Department of Applied Physics, Chalmers University of Technology, 412 96, Gothenburg, Sweden
[d] Sandvik Additive Manufacturing, 811 81, Sandviken, Sweden
[e] Department of Mechanical and Mechatronic Engineering, Waterloo University, Waterloo, Canada

ARTICLE INFO

Keywords:
Additive manufacturing
Electron beam-powder-bed fusion
Melting strategy
Grain structure
Alloy 718

ABSTRACT

This study presents a unique melting strategy in electron beam-powder bed fusion of Alloy 718 to tailor the grain morphology from the typical columnar to equiaxed morphology. For this transition, a specific combination of certain process parameters, including low scanning speeds (400–800 mm/s), wide line offsets (300–500 μm) and a high number of line order (#10) was selected to control local solidification conditions in each melt pool during the process. In addition, secondary melting of each layer with a 90° rotation with respect to primary melting induced more vigorous motions within the melt pools and extensive changes in thermal gradient direction, facilitating grain morphology tailoring. Four different types of microstructures were classified according to the produced grain morphology depending on the overlap zone between two adjacent melt pools, i.e., fully-columnar (overlap above 40 %), fully-equiaxed (overlap below 15 %), mixed columnar-equiaxed grains, and hemispherical melt pools containing mixed columnar-equiaxed grains (overlap ~20–25 %). The typical texture was <001>; however, the texture was reduced significantly through the transition from the columnar to equiaxed grain morphology. Along with all four different microstructures, shrinkage defects and cracks were also identified which amount of them reduced by a reduction in areal energy input. The hardness was increased through the transition, which was linked to the growth of the γ" precipitates and high grain boundary density in the fully-equiaxed grain morphology.

1. Introduction

During solidification of a molten material, there are different phenomenon that occur simultaneously, which strongly affect the hierarchical microstructure of the alloy. These phenomenon consist of heat flow and fluid flow driven by complex set of facts, such as mass gradient due to the transport of solutes via elemental segregations, thermo-capillary forces generated due to the surface tension variation and large temperature gradients across the molten metal surface [1–4]. Tailoring the microstructure is of great interest for the prediction of the mechanical properties of materials. Control of the local microstructure determined during solidification also affects the mechanical properties and functional performance of the manufactured part [1]. The main solidification parameters affecting the microstructure in the local liquid-to-solid transformation are temperature gradient (G), cooling rate ($\dot{T}$), and solidification rate (R), which are dependent on each other. It should be noted that the ability to control such parameters strictly depends on the solidification condition applied by the process setting [2,5,6]. These parameters change during solidification and are highly dependent on various factors, in which one is the melt pool geometry that is a function of manufacturing process parameters in powder bed fusion processes, such as scanning speed and beam current. Generally, the solidification parameters can result in two types of grain morphology, including columnar or equiaxed grains. The nucleation of crystals in a melt pool with an undercooled isothermal condition leads to an equiaxed morphology if the growth of the crystal is equal in all directions. The morphology is identified as columnar when a unidirectional heat flux is applied. For the formation of the equiaxed grains in

* Corresponding author.
E-mail address: paria.karimi@hv.se (P. Karimi).

https://doi.org/10.1016/j.msea.2021.141820
Received 31 March 2021; Received in revised form 1 July 2021; Accepted 26 July 2021
Available online 27 July 2021
0921-5093/© 2021 The Authors. Published by Elsevier B.V. This is an open access article under the CC BY license (http://creativecommons.org/licenses/by/4.0/).

the undercooled growth condition, the liquid temperature needs to be below the liquid/solid interface temperature. This can happen by cooling the liquid under its equilibrium transformation temperature or by elemental segregation, which causes solute enrichment in the liquid ahead of the growing liquid/solid interface (i.e., constitutional supercooling) during solidification [7]. In the columnar growth condition, the direction of heat flux is from the high-temperature melt zone to the low-temperature solid. A columnar-to-equiaxed grain morphology transition is triggered if the equiaxed grains nucleation happens in the liquid zone ahead of the columnar grains [5].

In addition to the grain morphology, texture or crystallographic orientation can also significantly affect the material properties, including ductility and strength. Moreover, the texture has a dependency on grain boundary networks; therefore, efforts have been accomplished to engineer the grain boundaries to control the texture and hence the material properties [8,9]. However, conventional manufacturing techniques, such as casting and welding, have limitations in tailoring the site-specific grain morphology and texture because of the difficulties in controlling the heat transition at very short length scales. The great potential of the additive manufacturing (AM) technology for controlling the local solidification, thus tailoring the grain morphology and texture in the production of novel engineering parts, is a major benefit compared to conventional manufacturing technologies [3, 10–16]. In particular, there has been a growth in research interest regarding electron beam-powder bed fusion (EB-PBF) as a potential technique for manufacturing geometrically-complex materials with a tailored microstructure [17,18]. Moreover, EB-PBF can accurately control the microstructure during melting and facilitates adjusting the microstructure by altering the solidification parameters.

A few strategies have already been investigated, mainly in Alloy 718, by adjusting the process parameters to interrupt the primary thermal gradient and growth directions, which are parallel to the build direction. The interruption provides the ability to control the solidified microstructure of the material in EB-PBF [6,8]. Dehoff et al. [19] showed that a spatially-controlled crystallographic texture in Alloy 718 can be achieved using a multispot melting strategy. Helmer et al. [20] showed that by increasing the scanning speed at lower line offset values, dendrite fragmentation occurs, in which the fragmented dendrites act as nucleation sites for the new grains; hence, the grain morphology can be tailored [21]. The local temperature gradients and solidification growth rates at the liquid/solid interfaces are significantly affected by the EB-PBF process parameters. It has been reported that the solidification morphology of Alloy 718 was significantly affected by the beam scanning strategies in each layer [8,21]. There are still challenges in the fundamental understanding of the above strategies because customized melt themes were used instead of the typical melting theme recommended by the machine supplier (i.e., Arcam-EBM). Hence, the goal of the present research was to explore microstructure evolution using a unique melting strategy in a specific range of scanning speed, beam current, line offset, and line order number (the order of line's melting) with respect to the machine supplier's recommended melting theme. In this work, the microstructural characteristics, such as grain structure (morphology and texture), primary dendrite arm spacing, average total length of cracks and strings of shrinkage defects, hardness, and size of the γ" precipitates were investigated with respect to changes in the process parameters of the proposed melting strategy.

2. Materials and methodology

Alloy 718, which is a nickel-iron-based superalloy with a nominal composition of 53.30Ni-18.7Cr–3Mo-5.1Nb-0.9Ti-0.4Al-0.01Co-0.07Mn-0.001Si-0.028C-balance Fe (all in wt%) was used as the feedstock powder provided by Sandvik AB (Sandviken, Sweden). The powder particles were produced by vacuum induction melting and subsequent inert gas atomization using argon gas and sized to a powder particle size distribution of 45–106 μm. The powder particles were in both irregular and spherical shapes, with some fine satellite particles attached to the coarser ones.

Nine cubic samples with a similar dimension of 15 × 15 × 10 mm^3 were manufactured using an A2X machine (Arcam-EBM|a GE Additive, Mölnlycke, Sweden) to evaluate the process parameters. All cubes, shown in Fig. 1, were built using an accelerating voltage of 60 kV under a controlled pressure of He set at 2×10^{-3} mbar, a layer thickness preset at 75 μm, and a focus offset of 15 mA. The control software of version 4.2.76 supplied by Arcam was used. A comprehensive description of the EB-PBF process can be found in Refs. [10,11,22–24]. A 10-mm-thick polycrystalline stainless steel build plate was used. The scanning strategy was in a snake-like manner with a line order number of 10 (melting 1st, 11th, 21st line, and so on, then melting 2nd,12th, 22nd, and so on); see Fig. 1a. The main reason to select the high line order number of 10 was due to its high potential to support local solidification conditions at low scanning speed by giving sufficient time for each melt pool to be semi-solidified before re-melting again [25]. The scanning direction was rotated by 90° after every layer. In the melting strategy developed in this work, each layer was melted twice; however, no powder was spreaded before the second melting; see Fig. 1a. Thus, the powder raking, sintering, and post-heating were not activated in the secondary melting; therefore, the process time was not altered significantly. The process parameters, such as scanning speed, beam current, and line offset in the second melting, were similar to the primary melting. The main idea behind adding the secondary melting in each layer was to boost more interruptions at the melt pools to create a higher chance for dendrite fragmentations/grain detachment mechanisms inside the melt pools for nucleation of more grains. It is worth noting that the above process window without the secondary melting was unable to trigger the columnar to equiaxed transition in the preliminary trials of this work.

The samples were manufactured based on a full factorial screening design of experiments (DoE) using MODDE 12 (Umetrics, Umea, Sweden) software in two levels for each parameter; see Table 1. The same selected process window was repeated one more time to see the repeatability of the results as well. Moreover, a wider line offset (i.e., the distance between two adjacent scanning lines) range from 300 to 500 μm was used compared to the Arcam recommended value (125 μm) to increase the spread of the melt pools and further facilitate the nucleation of new grains along the melt pool boundaries. During manufacturing, the melting process for a number of layers from each cube was recorded using a digital single-lens reflex (DSLR) camera (Nikon D3500, Sendai, Japan) which was located out of the chamber close to the glassy window of the machine; see Fig. 1b. The photos were used to show the effect of the secondary melting, wide line offset, and high line order number in the separation of the melt pools from each other.

For microstructural characterization, each sample was cut from the middle in a direction parallel to the build direction. One-half of the samples was metallographically prepared (mounting and grinding/polishing) to examine the grain structure, melt pool geometry, primary dendrite arm spacing (PDAS), and content of defects (e.g., cracks and shrinkage defects). The mounted samples were ground and polished metallurgically using SiC papers up to 2500 grit and a 0.05-μm silica suspension, respectively. The polished cross-sections were electrolytically etched with 10 wt% oxalic acid at room temperature and 3 V for 5–10 s to reveal the melt pool depth/width and dendrite arms in the uppermost layers. The grain structure of the samples was analyzed using an Ultra Zeiss field emission scanning electron microscope (FE-SEM, EVO 50, Oxford, the United Kingdom) in the backscatter electron (BSE) mode operating at an accelerating voltage of 15 kV. Both SEM and a Zeiss light optical microscope (LOM) (Axio Imager 2, Cambridge, UK) were used to evaluate the PDAS, shrinkage defects, and cracks of the as-built samples manufactured using various process parameters. Sixteen LOM images were acquired from a similar area in each sample with a horizontal field width of 2.5 mm to determine the effect of the process parameters on the content of defects. The average total crack and total shrinkage lengths were then measured by the image analysis (IA)

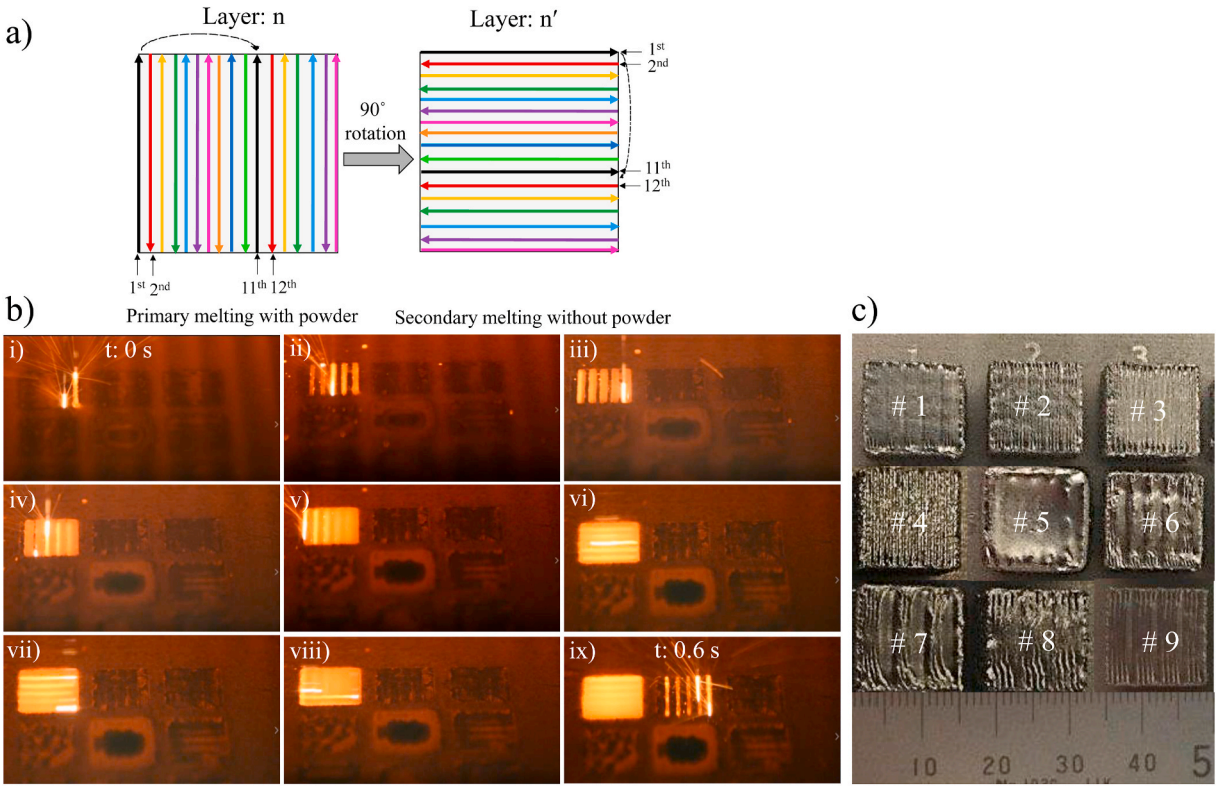

Fig. 1. a) Schematic of the proposed melting strategy illustrating the primary and secondary melting in each layer with a line order number of ten, b) high-resolution DSLR camera photos taken during the melting process, showing the novel scanning strategy in the EB-PBF process, and c) top view of the as-built samples.

Table 1
Detailed process parameters used in the EB-PBF process.

Sample #	Scanning speed (mm/s)	Beam current (mA)	Line offset (μm)	Energy per area = Beam current × VoltageScanning speed × Line offset (J/mm^2)
1	400	10	300	5.0
2	800	10	300	2.5
3	400	10	500	3.0
4	800	10	500	1.5
5	400	15	300	7.5
6	800	15	300	3.75
7	400	15	500	4.5
8	800	15	500	2.2
9	600	12.5	400	3.1

technique, ImageJ software [26]. In this work, due to the linear morphology of the shrinkage defects, the average total shrinkage length was defined as TSL and was used to compare different samples quantitatively. The SEM images of the polished samples with a horizontal field width of 400 μm were used to quantify the PDAS. A detailed description of the PDAS measurements using the ImageJ software can be found in previous studies [13,24]. The electron backscatter diffraction (EBSD) system (GAIA3-TESCAN, Oxford, UK) performing at an accelerating voltage of 20 kV was used to evaluate the effect of the process parameters on the grain morphology and texture. The EBSD mappings of four control samples were obtained using a step size of 2 μm and analyzed with HKL Channel 5 software. Vickers microhardness (HV) indentations were performed in a similar area in each sample using a Shimadzu microhardness tester (HMV-2, Kyoto, Japan). The applied load and dwell time for each point were 500 g and 15 s, respectively. Twenty-five indentations were conducted in each sample to provide the average hardness and standard deviation values.

Thin foils from a direction parallel to the build direction were prepared for transmission electron microscopy (TEM). In the first step, the samples were mechanically thinned down to a thickness of ~100 μm. Then, discs with a diameter of ~3 mm were punched out from the samples. The discs were further thinned mechanically to 10–20 μm using a Gatan dimple grinder (model 656, Gatan Ltd., Corby, Northans, UK). Later, ion beam milling was conducted on the thin samples to reach electron transparency, using a Gatan precision ion polishing system (PIPS) (model 691, Gatan Ltd., Corby, Northans, UK). The thin foils were characterized using a JEOL field emission TEM (JEM. 2010F, Tokyo, Japan) operating at an accelerating voltage of 200 kV. The length of the precipitates was estimated by the IA technique. For each sample, five TEM images in the same height from the top and bottom of the samples were taken, and for each image, approximately 20 precipitates were considered to enable proper estimation of the length of the γ" precipitates. Furthermore, selected area diffraction (SAD) patterns were used to determine the crystal structure of the γ matrix and the γ" precipitates. In addition to the TEM analysis, small-angle X-ray scattering (SAXS, SAXSLab Mat:Nordic instrument with a Rigaku 003+ high-brilliance microfocus Cu-radiation source) was performed to quantitatively analyze the size of the γ" precipitates in various conditions. For SAXS, very thin foils with a thickness of less than 50 μm were prepared from the samples, and eight locations per sample (in a similar location in all the samples) were examined; the γ" size was extracted and reported as the radius of gyration based on the Guinier approximation [27]. To capture 3D images of the cracks and shrinkage defects, X-ray computed tomography (XCT) was performed using a ZEISS Xradia 520 Versa (ZEISS, Oberkochen, Germany) at 140 kV and 10 W, with an exposure time of 1 s per 2D slice, at a resolution (voxel size) of 2 μm. For this analysis, a small cubic sample with a dimension of 1 × 1 × 2 mm^3 was extracted from each sample in the same location. The 2D projections were rebuilt to a 3D image applying a beam hardening of 0.05 and examined in Dragonfly 3.1 (Object Research Systems (ORS), Montreal, Canada).

3. Results and discussion

3.1. Grain structure; morphology and texture

Fig. 2 shows an overview of the grain morphologies in a full transverse view, from one edge to the other edge of the samples. Each of these images consisted of five SEM images taken (with the field width of 4 mm) from a location approximately 3 mm from the top and bottom of the samples manufactured using various process parameters, according to Table 1, and stitched together to provide the overall view. Samples #1, 3, 5, 6, and 7 presented a columnar grain morphology, and only sample #2 showed the hemispherical melt pools with mixed grain morphology. In the entire process window, only sample #4 showed a fully-equiaxed grain morphology, and two samples (#8 and 9) consisted of the mixed columnar-equiaxed grain morphology.

Fig. 3 shows the representative grain morphologies achieved in samples #1, 2, 4, and 9 at a higher magnification. To better understand the mechanisms involved in the columnar-to-equiaxed grain morphology transition, various characteristics of the microstructure, such as the PDAS, overlap zone between two adjacent melt pools and depth-to-width ratio in the melt pools were measured, and the results are provided in Table 2. The grain morphologies observed in various process conditions can be understood as follows:

i) Fully-columnar: this morphology was formed due to the epitaxial growth of the grains because of the very steep thermal gradient along the build direction; see Fig. 3a. This morphology has been commonly observed in the EB-PBF-manufactured material [11, 13,24].
ii) Hemispherical melt pools with mixed morphology: this grain morphology was observed in sample #2, where the overlap zone between the melt pools was approximately 20–25 %, which resulted in a grain morphology similar to the grain morphology in a solidified weld pool [1]; see Fig. 3b.
iii) Fully-equiaxed: in sample #4, with a fully-equiaxed grain morphology, the energy input was the lowest (1.5 J/mm^2), and only approximately 15 % of the previous adjacent melt pool was re-melted. The combination of the low overlap between the

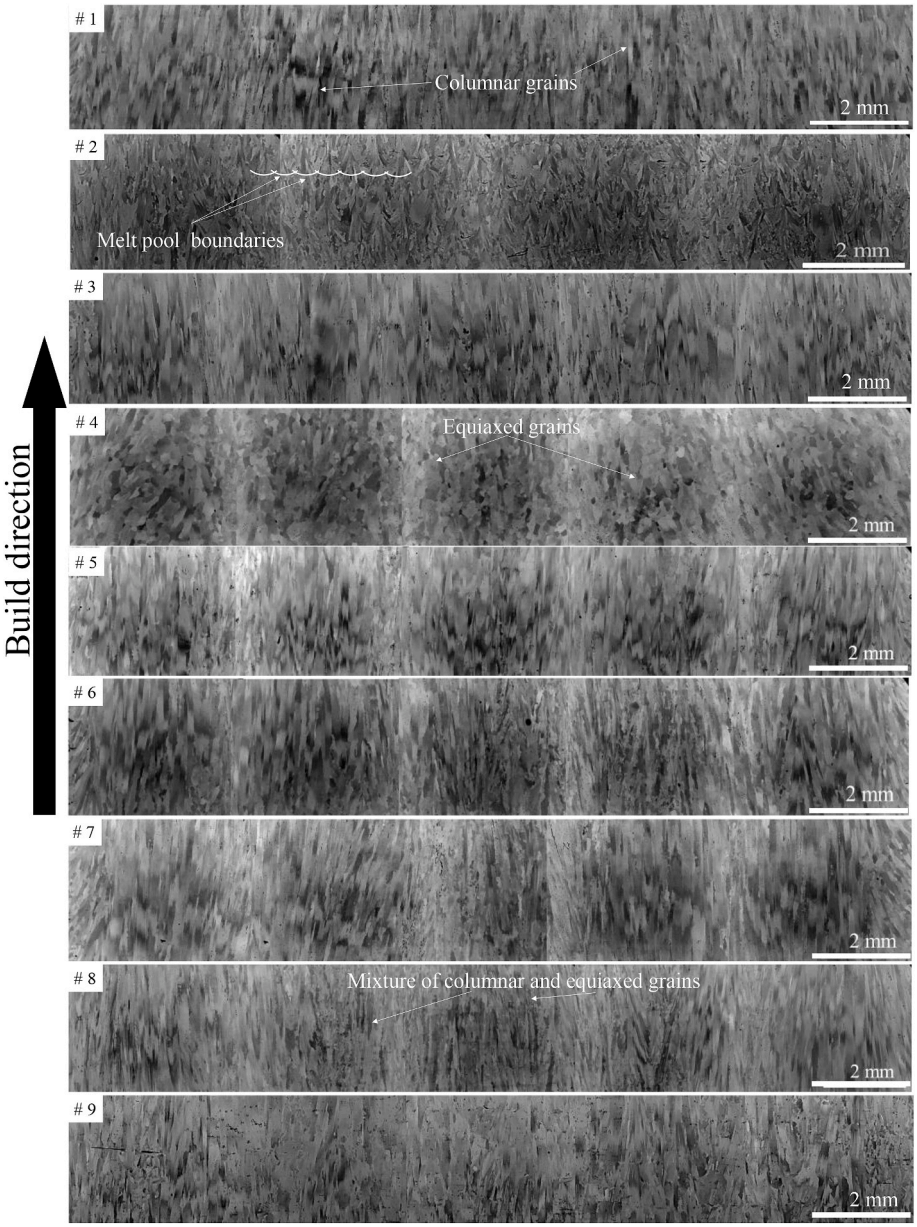

Fig. 2. SEM images (BSE mode) of the grain morphologies in various process conditions.

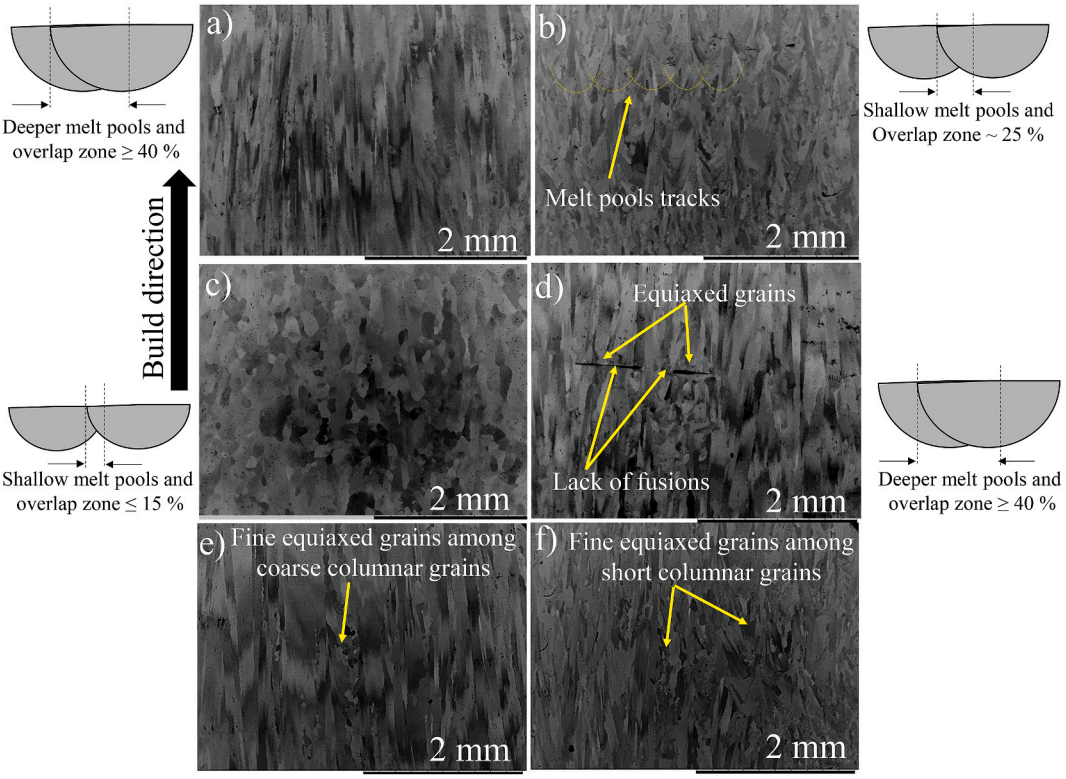

Fig. 3. High-magnification SEM images (BSE mode) of the grain morphologies formed in the representative samples; a) sample #1 (fully-columnar), b) sample #2 (hemispherical melt pools with mixed morphology), c) sample #4 (fully-equiaxed), d) sample #9 (a mixture of equiaxed and columnar grains), e-f) sample #8 (a mixture of equiaxed and columnar grains).

Table 2
Measured responses (PDAS, corresponding cooling rate, type of grains, melt pool depth/width ratio, the overlap between two adjacent melt pools, Avg. TCL, and Avg. TSL) with respect to various sets of process parameters.

Sample #	PDAS (μm)	Corresponding cooling rate (°C/s)	Type of grains	Depth/width melt pool ratio (~)	Overlap between two adjacent melt pools (~%)	Avg. TCL (μm)	Avg. TSL (μm)
1	11 ± 1	1362	Columnar	0.2	65	177	179
2	7 ± 1	4877	Hemispherical melt pool with mixed morphology	0.6	25	11	45
3	10 ± 1	1882	Columnar	0.1	41	158	86
4	5 ± 1	11429	Equiaxed	0.5	15	18	24
5	14 ± 3	736	Columnar	0.2	52	129	205
6	11 ± 2	1264	Columnar	0.3	57	78	82
7	12 ± 2	906	Columnar	0.2	45	166	146
8	10 ± 1	1815	Mixed	0.3	41	36	25
9	8 ± 2	3303	Mixed	0.2	44	40	77

adjacent melt pools and low re-melting of the underlying layers promoted the formation of the equiaxed grains; see Fig. 3c. In fact, by nucleation of the equiaxed grains ahead of the columnar grains front, a sudden columnar-to-equiaxed grain transition parallel to the build direction is provoked.

iv) Mixed (co-existence of) equiaxed and columnar grains: the dominant grain morphology was still columnar; however, some equiaxed grains were also formed among the columnar grains. The formation of the mixed grain morphology can be due to the presence of rows containing defects, such as the lack-of-fusion (LoF) defects shown by a yellow arrow in Fig. 3d. The area around these defects is susceptible to the nucleation of new grains because of interruptions in the path of the steep thermal gradient. However, there were some fine equiaxed grains among the columnar grains, which formed due to *in situ* recrystallization at the grain boundaries; see Fig. 3e and f. In fact, by employing the line order number function and secondary melting of each layer, each single scan line was melted and re-melted promptly with different melting return times. This results in significant residual stress and lattice strain as well as high stored energy, which facilitates the nucleation of the new grains [25]. This phenomenon was observed in a previous work, where *in situ* recrystallization occurred when the line order number function was increased [24]. Indeed, *in situ* recrystallization is the mechanism by which dislocation rearrangements form low dislocation density regions [29], and it is attributed to the free energy stored in the dislocations that are not entirely released after recovery. The developed melting strategy in this work with the intrinsic cyclic heat treatment through melting a layer several times could provide this phenomenon to happen.

Understanding the grain evolution and transition from the columnar to equiaxed morphology is important for controlling the grain structure during solidification. The grain structure tailoring in the EB-PBF process

has been investigated in a few studies, and some mechanisms have been proposed [6,20,30]. In fact, the columnar grain morphology as a result of directional solidification was identified by an enforced steep thermal gradient through the melted layers. The columnar morphology is supposed to appear at a certain amount of undercooling [1]. The formation of the equiaxed grains in EB-PBF process was reported to be through heterogeneous nucleation, grain detachment or dendrite fragmentation mechanisms [20,21]. The heterogeneous nucleation may happen at any moment during solidification because of constitutional supercooling. The dendrite fragmentation/grain detachment can happen during the local variation in the temperatures or solute concentration due to the convective fluid flow, where partial grain melting and free secondary arms act as nucleation sites for new grains [31]. The rejection of niobium-rich solute in Alloy 718 and increase in solute concentration ahead of the dendrite tips promotes the formation of the equiaxed grains, which eventually facilitates the columnar-to-equiaxed grain morphology transition. In fact, the rejection of the niobium-rich solute into the solidification front results in a lower liquid temperature than the liquid-solid interface temperature, which increases the undercooling area at the columnar front. If the undercooled area is large enough, the growth of the columnar dendrites will be hindered, and the columnar-to-equiaxed grain morphology transition will be facilitated [32].

One affecting factor on the grain morphology related to the amount of undercooling is the cooling rate ($\dot{T}$) from the liquid to the solid state. As Table 2 shows, the cooling rate was estimated from the average PDAS values (from 30 measurements at the most upper layers) in each sample [33]. The cooling rate in the course of the solidification of a dendritic microstructure can be predicted using Eq. (1) [33,34];

$$\lambda = A\,\dot{T}^{-n} \tag{1}$$

where λ (μm) is the PDAS, and A (μm) and n (dimensionless) are proportionality factors associated with the material. A and n were calculated as 122.6 μm and 0.342, respectively, for Alloy 718 [35]. According to the welding literature, a higher cooling rate results in the formation of a much finer microstructure, which increases the chance of the formation of the equiaxed grains [35]. In sample #4 with the fully-equiaxed morphology, the cooling rate was the highest.

The melt pool geometry, as an affecting factor on the grain structure, was evaluated. The width and depth of the melt pools measured using LOM were found in the range of 600–1250 and 285–525 μm, respectively. These results mean that 3 to 6 underlying layers were re-melted while melting a new layer; see Fig. 4. Considering the line offset of 300–500 μm, approximately 15–80 % of one melt pool was re-melted while adding a new melt pool in the same layer. With the applied melting strategy, where the overlap between two adjacent melt pools was less than 15 %, the grain morphology had a higher tendency for the formation of the equiaxed grains. Generally, the equiaxed grains grow ahead of the columnar front and the columnar-to-equiaxed grain morphology transition occurs when the size and amount of the equiaxed grains are adequate to hinder the advancement of the columnar front [20]. With an overlap of approximately 25 %, the hemispherical melt pools with mixed grain morphology were detected, see sample #2 in Fig. 4. The melt pool width was approximately 665 μm, the line offset was 500 μm, and the re-melted overlap was calculated to be 25 % in sample #2. As the etched cross-section in Fig. 5a shows, the individual melt pool was almost visible, with a few sharp elongated columnar grains at the center of the melt pool bottom. The grains inside each melt pool grew toward the center of the melt pool, and their morphology was affected by two heat flux directions, i.e., one parallel to the build direction (center of the melt pool bottom), and another toward the melt pool boundary (shown in Fig. 5b). The final grain morphology was defined in a trade-off between the two heat fluxes. In the samples with the hemispherical melt pools with mixed morphology, there were regular regions with fully-fine equiaxed grains, as shown in Fig. 5a. From the height of those regions and the preset layer thickness of 75 μm, it seems that five underlying layers were affected during the melting of a new layer. In the overlap zone range greater than 40 %, either columnar or mixed grain morphology was formed, which was linked to the induction of a strong thermal gradient along the build direction.

Grain texture, as an important factor affecting the level of anisotropy in the material properties, must be taken into consideration in addition to the grain morphology [36]. Fig. 6 shows the texture of four different types of microstructure along the build direction from the EBSD analysis in the inverse pole figure (IPF) and pole figure (PF) mappings. According to the EBSD mapping, the texture was strong in the <001> crystallographic direction in the fully-columnar grain morphology, which is the preferred growth direction in a FCC crystallographic structure [11,13]. The multiple of uniform density (MUD) quantified as the degree of the

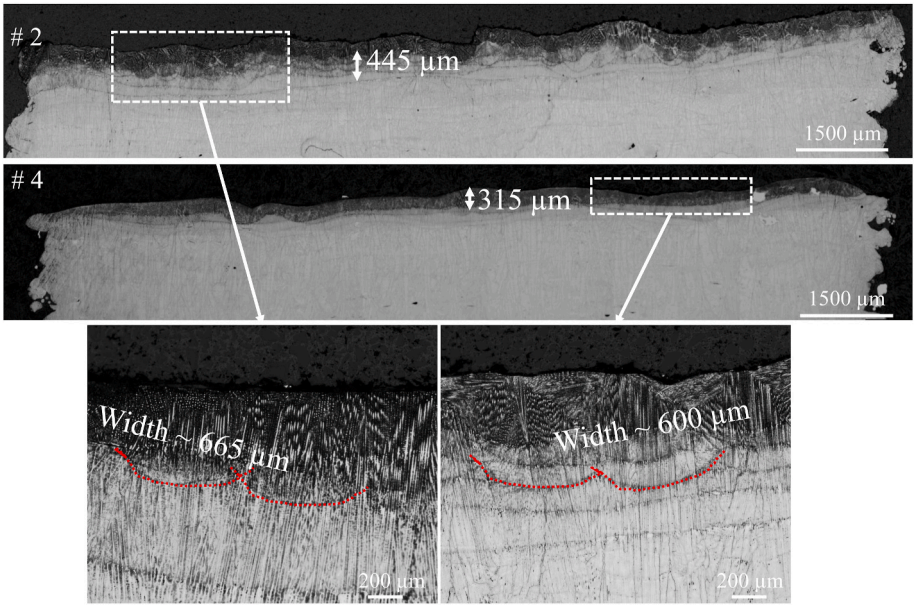

Fig. 4. LOM images of the melt pool geometry in sample #2 with the hemispherical melt pools with mixed morphology and in sample #4 with the fully-equiaxed grain morphology.

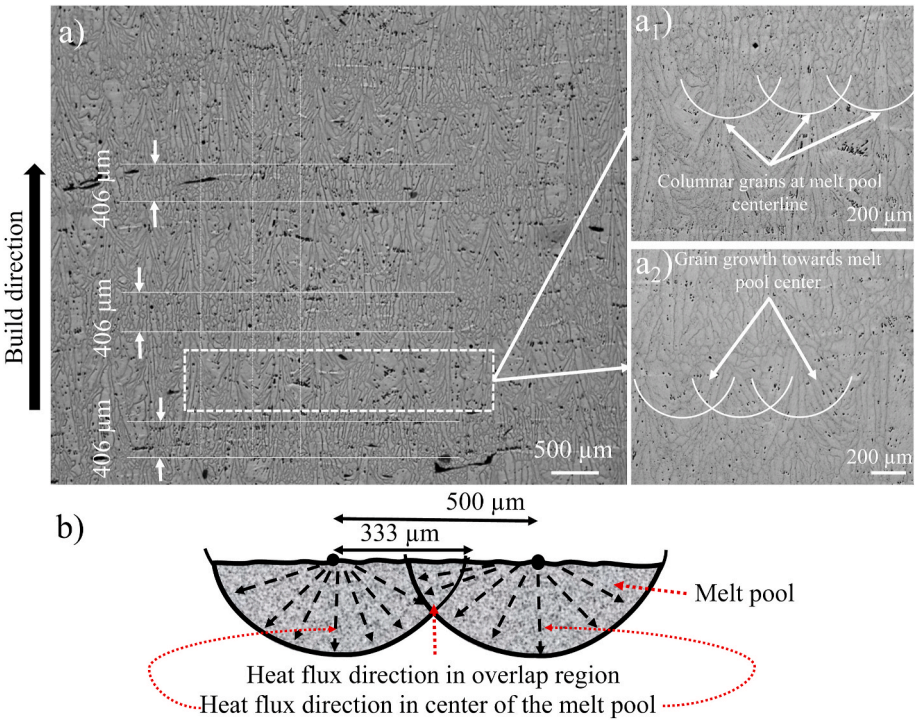

Fig. 5. a) LOM images of sample #2 with hemispherical melt pools with mixed morphology and b) schematic of the melt pools with the overlap zone.

peak strength in the pole figures illustrates the number density of crystals aligned in a crystalline orientation. In a fully-columnar grain morphology, the MUD value was in the range of 35–38; see Fig. 6, which was very similar to the range of the MUD values in samples manufactured using the Arcam recommended theme [11]. In the mixed grain morphology, the texture was decreased significantly because of the formation of some equiaxed grains in random locations. Later, in the hemispherical melt pools with mixed morphology, the texture was further decreased because there were more equiaxed grains with different crystallographic directions. Finally, sample #4 with the fully-equiaxed grains showed the lowest texture; see Fig. 6. As depicted in the pole figures and the MUD values in the fully-equiaxed grain morphology, the texture was not random due to the presence of a few columnar grains (the aspect ratio was above 3) in the <001> direction, which caused the MUD to be above one. The reduction of the texture can be influenced by the solidification conditions in each process setting. Typically, a steep thermal gradient and low growth rate lead to a strong texture [19,19,36]. In this study, the texture was further reduced by reducing the overlap zone between the melt pools in the selected process window and inducing more interruptions via the secondary melting of each layer.

3.2. Defects: types, content, and formation mechanisms

To better visualize the characteristics of different defects in a 3D mode, the micro-CT analysis was performed as shown in Fig. 7, where the color represents the equivalent volume of the fifty largest defects. Apart from the commonly-observed round pores, mainly originated from the feedstock powder [23], and the LoF defects, typically occurred due to the low amount of applied energy input, two other linear-type defects (longer than 50 µm in length) were observed in the samples using both XCT and LOM. These defects were divided into two groups according to their formation mechanisms and their morphologies; i) thermal shrinkage defects with round-shaped start and end points, as well as curved edges along the defects, and ii) cracks with sharp start and end points, as well as straight edges along the defects. The average length of these defects was measured as the total shrinkage length (TSL) and total crack length (TCL), see Table 2. The defect volumes in the samples with the lowest level of TSL and TCL (given in Table 2) were found in the samples with the hemispherical melt pools containing mixed and equiaxed grain morphology, which were in the range of 0.00015–0.00071 mm^3 and 0.00015–0.0006 mm^3, respectively with a coefficient of variation (a ratio of average value to standard deviation) of 3–5%.

Theories regarding the formation of the solidification defects in the conventional manufacturing processes, such as casting, and welding can still be relevant and valid for AM. However, it remains challenging to determine and confirm the intrinsic mechanisms in AM because of the extremely localized and dynamic solidification condition, where melting, re-melting, fluid flow, material evaporation, and spattering jets of molten metal occur simultaneously.

According to the literature, the thermal shrinkage defects occur as a result of the volume reduction of the melted material during cooling and solidifying [10,13,22,37]. The shrinkage defects form because of volumetric differences between the solid and liquid phases during solidification [37]. In this work, the linear shrinkage defects were mainly dendritic-type according to their morphology, which were narrow and thin with some finer cavities in their neighborhood; see Fig. 8a. There are two contradictive theories regarding the level of the shrinkage defects at higher energy input [13,23,38–40]. According to the first theory, larger melt pools form at higher energy input, and the melt pool boundaries are susceptible to shrinkage defects because of the accelerated cooling rate in these regions [13,39]. However, according to the second theory, increasing the energy input and subsequently creating larger melt pools reduce the cooling rate from the liquid to the solid state in the entire liquid metal, which prevents the formation of the shrinkage defects [13,40,41]. The shrinkage defects are reduced because there is sufficient time for the liquid to fill the last areas to be solidified in the interdendritic regions. This means that a raise in the intergranular liquid film reduces the stress/strain needed to lead decohesion at the solid-liquid interface. It should be considered that by increasing the melt pool size, the temperature variation will increase locally, which can add thermal stress; however, because of the high-temperature nature of the EB-PBF process, the level of residual stress is generally low. In fact, at

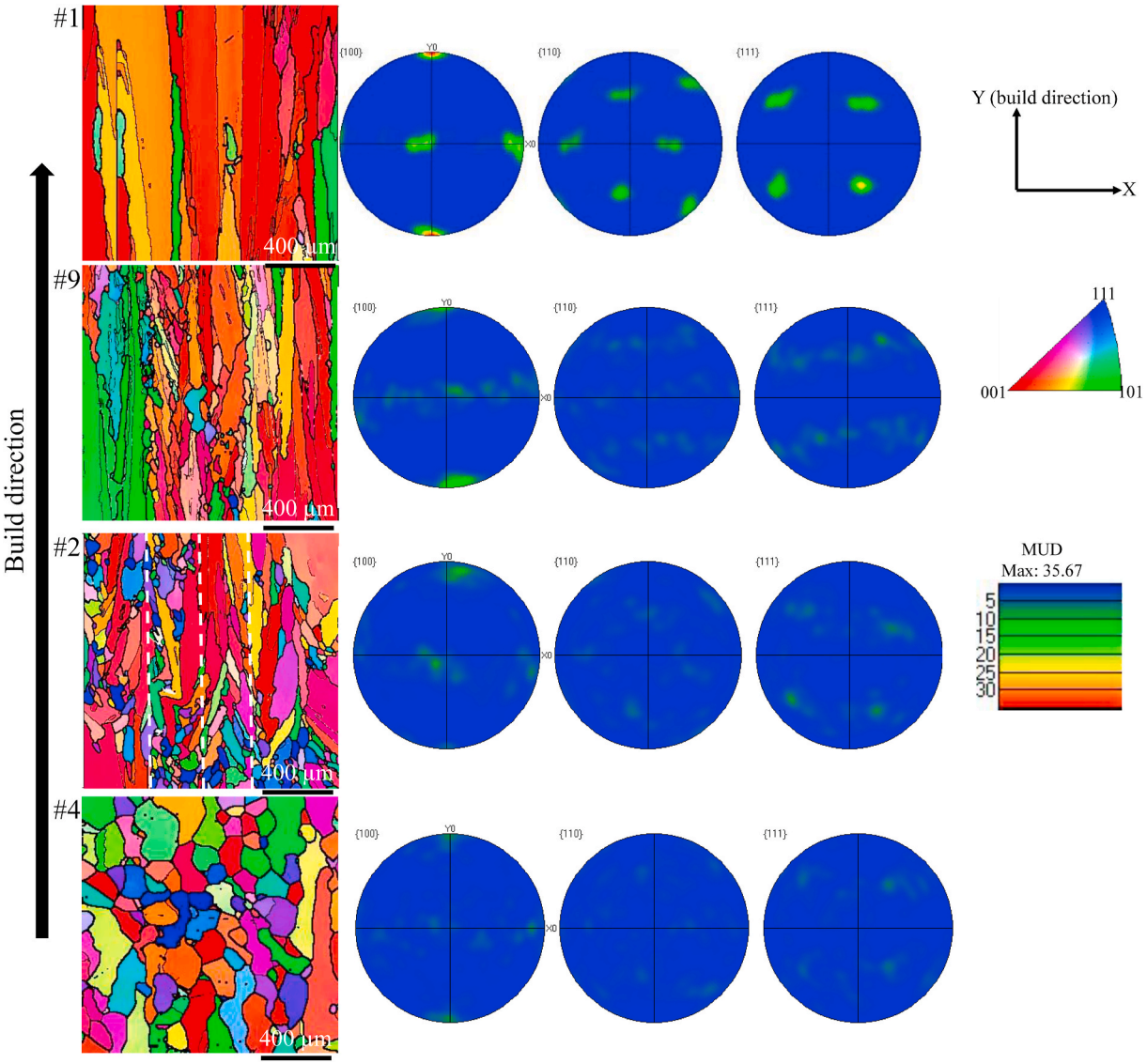

Fig. 6. EBSD-IPFs and PFs mapping of the grain morphologies along the build direction in various conditions; a) sample #1: fully-columnar morphology, b) sample #9: mixed grain morphology, c) sample #2: hemispherical melt pools with mixed morphology, and d) sample #4: equiaxed grains morphology.

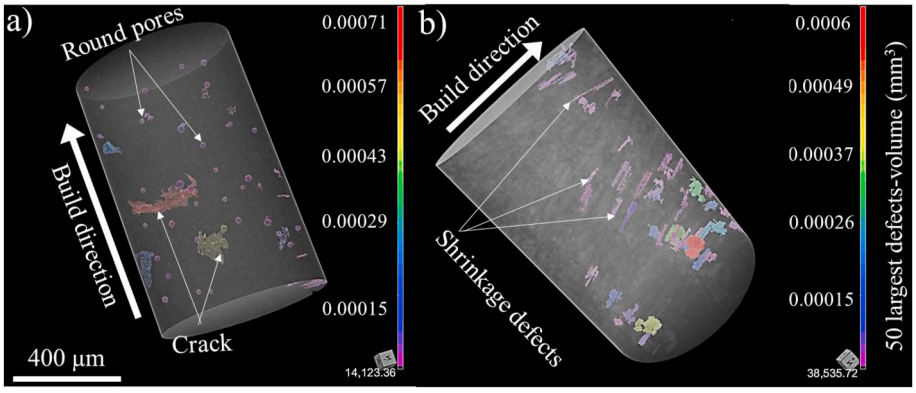

Fig. 7. X-ray computed tomography (XCT) showing the defect distribution in a) sample #2 with the hemispherical melt pools with mixed morphology and b) sample #4 with the equiaxed grain morphology.

high energy input, thermal distortions are identified as a probable source for the shrinkage defects because of the applied thermal stresses at elevated temperatures [42]. In addition, cyclic heating and cooling by fully- and partially re-melting of the same layer by the addition of new layers can induce more thermal stresses, which can reinforce the formation of the shrinkage defects [43]. The values of the average total

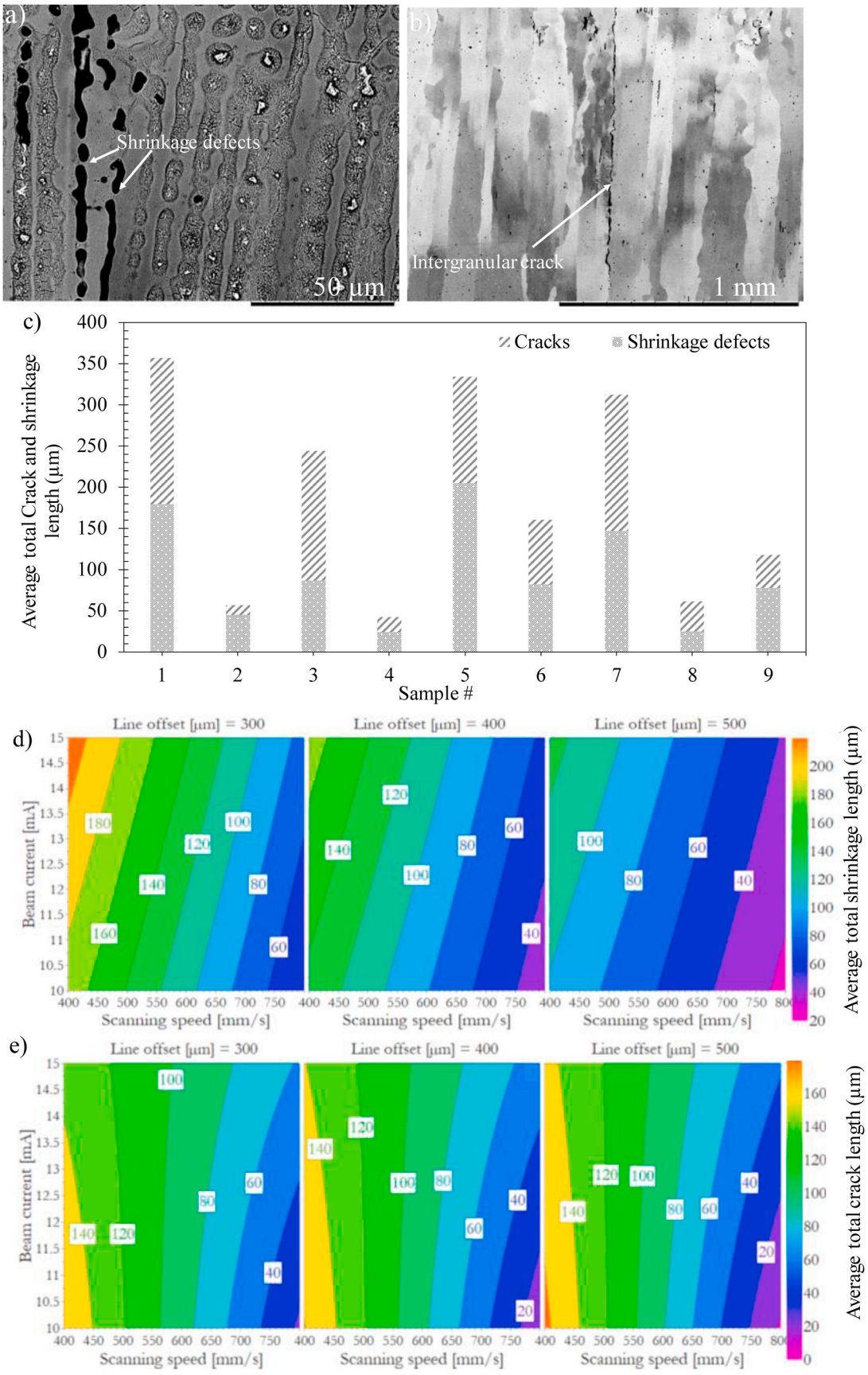

Fig. 8. a-b) Higher magnification of the defects in samples #1 and 9, c) measured average total shrinkage and crack length in different samples, and d-e) 4D contour graphs from the DoE software.

shrinkage defects in the samples manufactured using various process parameters are given in Fig. 8c. The most effective parameters in reducing the shrinkage defects were the scanning speed and the line offset. As the scanning speed was increased, the level of shrinkage defects decreased. In addition, by increasing the line offset, a lower level of the shrinkage defects was detected; see Fig. 8d. Thus, according to the results of the present study, it can be confirmed that a higher scanning speed and higher line offset resulted in a lower energy input per volume (according to Eq. (2)) and subsequently formation of smaller melt pools, which led to a lower level of the shrinkage defects.

$$E = \frac{Beam\ current \times Beam\ voltage}{Scanning\ speed \times Layer\ thickness \times Line\ offset} \quad (2)$$

Cracks, as the second type of defects found in the samples, have different formation mechanisms and primarily result from thermal stresses during the manufacturing process [44–46]. According to the literature, Alloy 718 is known for its weldability. No cracks were observed when using Arcam recommended theme; however, the changes in process parameters to employ more interruptions at the melt pools for grain structure transition generate a significant amount of thermal stress needed for cracking. In this study, most of the critical cracks were formed along with the grain boundaries parallel to the build direction, as shown in Fig. 8b. Investigation around the grain boundaries did not show any sign of the Laves phase, which can be an indication for liquation cracking. Therefore, these cracks can be referred to as solidification cracks. The main mechanism behind the solidification cracking is that the thin film rich in solute, in the last step of solidification has inadequate strength to resist the contraction stresses caused during solidification [44,47,48]. These contraction stresses cause very large strains on the melt pool, which lead to solidification cracking. Moreover, during solidification, the solute segregation to the liquid phase reduces the eutectic temperature resulting in complete undercooling. This suggests that solidification cracking takes place in the last steps of solidification when the dendrites are close to fully-grown grains which are detached by a segregated element at the intergranular regions. Some phases formed from the segregated elements weaken the grain boundary.

The melt pool depth-to-width ratio is an important factor affecting the cracking susceptibility. A wide and low depth melt pool decreases the probability of solidification cracking; however, solidification cracking can still happen in a very wide melt pool. It is significantly important and critical to gain better control over the melt pool size. A depth-to-width ratio of 0.5 was found the best ratio in achieving the highest resistance against solidification cracking [34–37]. Table 2 shows the depth-to-width ratio of the melt pools and the average total crack length (TCL) values. The average total shrinkage length (TSL) was also measured in various process conditions, and the corresponding graph is plotted in Fig. 8c. The measured values were imported to the DoE software, and 4D contour graphs (three process parameters plus one response) are shown in Fig. 8e. It is evident that the highest scanning speed for all three different line offset values resulted in the lowest values of TSL and TCL. Moreover, by increasing the line offset at each specific scanning speed, TCL was decreased as well. This could be owing to the lower applied area energy, which caused the formation of shallow melt pools and, thus, a low risk of solidification cracking. In addition, the DoE design showed that the most significant parameter related to TCL is the scanning speed.

As mentioned earlier, the most critical factor affecting both the shrinkage defects and solidification cracks is the thermal stress, which is related to the solidification of successive layers. The melting and re-melting of each layer in the developed melting strategy cause a significant amount of thermal stress in the material. Indeed, during the manufacturing process, a layer in the manufactured part is subjected to tensile stress because the previously solidified layers restrict its shrinkage by contraction stresses. Moreover, as the liquid reaches the solidus temperature during the solidification, bridging happens between the secondary dendrite arms, which avoids the feed of liquid and causes the creation of solidification pores or cracks by means of the generated thermal stresses. The welding literature is again useful for understanding how thermally-induced stresses form and finally generate tensile stresses and solidification cracking [1,49]. In EB-PBF, multiple tracks in a snake-like scan strategy are needed to melt a layer with a certain amount of overlap between the tracks. The stress fields are assumed to be remarkably influenced by the implemented melting strategy. For example, some researchers have altered the melting strategy in the EB-PBF process to restrict the formation of thermally-induced stresses and, thus, solidification cracks [50,51]. In general, most of the cracks were internally located, primarily along the grain boundaries. High-angle grain boundaries (misorientation $> 15°$) are found sensitive to cracking, while low-angle grain boundaries (misorientation $< 15°$) stay intact, because low-angle grain boundaries can accommodate more strain before cracking via slip transmission and re-emission in adjacent crystals [44,48,52–54]. The EBSD analysis demonstrates that crack propagation always occurred in the intergranular mode, as shown in Fig. 9a. According to Fig. 9b, the fine grains were less susceptible to solidification cracking. In fact, refinement of the PDAS and the grains remarkably decreases the elemental segregation in the liquid channels and promotes extensive coalescence of the adjusting grains at the last step of solidification. This phenomenon mostly takes place due to a reduction in the sidelong growth distance of the grains with decreasing grains size, causing less solute concentration in the liquid channels [49,51]. It was found that reducing the PDAS can effectively decrease the elemental segregation in the interdendritic regions and promote early coalescence of the neighboring grains, which, in turn, avoid solidification cracking [47]. Solidification cracking occurs more readily in the coarse grains than the fine grains when the same thermal stresses are applied to the solidifying material. This primarily occurs because the critical strain along the grain boundary of the coarse grains is lower than that of the fine grains [52]. The results were in agreement with the fact that the resistance to hot cracking enhances when the grain boundary fraction enhances. The favorable effect of having fine grains with respect to the high resistance to solidification cracking is associated with the fact that the strain is distributed within more interfaces. It is worth noting that the cracks and shrinkage defects are reported as the common issues in the grain morphology tailoring [55], which could be expected when the solidification parameters are manipulated significantly to tailor the grain morphology. Such defects can be healed by thermal post-treatment, such as hot isostatic pressing, without altering the produced grain structure. Moreover, optimization of the processing parameters to manufacture defect-free samples with fine equiaxed grains is the topic of an ongoing research.

3.3. Micro-Vickers results for different grain structures

Hardness of the material is a crucial characteristic concerning the service life and durability. In this study, the microhardness was measured at the same height (~3 mm) from the top and bottom of the cubic samples in the pre-defined process window. According to Fig. 10a, the sample with the equiaxed grain morphology showed the highest hardness, followed by that of the hemispherical melt pools with mixed morphology. There are several affecting factors on the hardness of Alloy 718 which consist of the grain size; as the grain boundaries can act as a barrier for dislocation movement during deformation [56], and the size of the Nb-rich carbides because if the carbides become coarse, they can consume Nb that is required for the formation of γ" as the main strengthening phase. Therefore, the size of the γ" precipitates was investigated in the samples manufactured with different grain morphologies and the results are shown in Fig. 10b–d. In fact, due to the lattice misfits between the γ matrix and the γ" precipitates, lattice distortions and coherency strains are expected, which affect the strengthening mechanism and hardness of Alloy 718 [57–59]. A regular network of the γ" precipitates shown in Fig. 10b–d, was established and

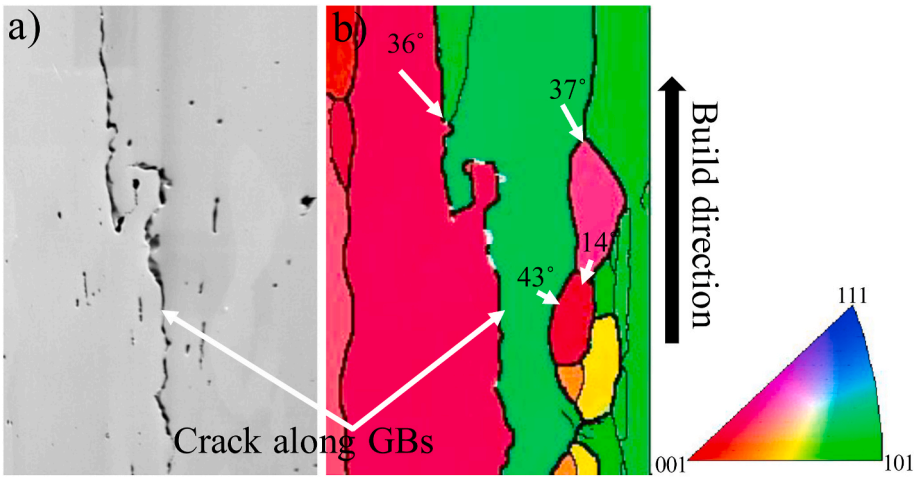

Fig. 9. a) SEM-BSE image of a crack along with the grain boundary, b) IPF-EBSD map illustrating misorientation along with the high-angle grain boundaries in sample # 1.

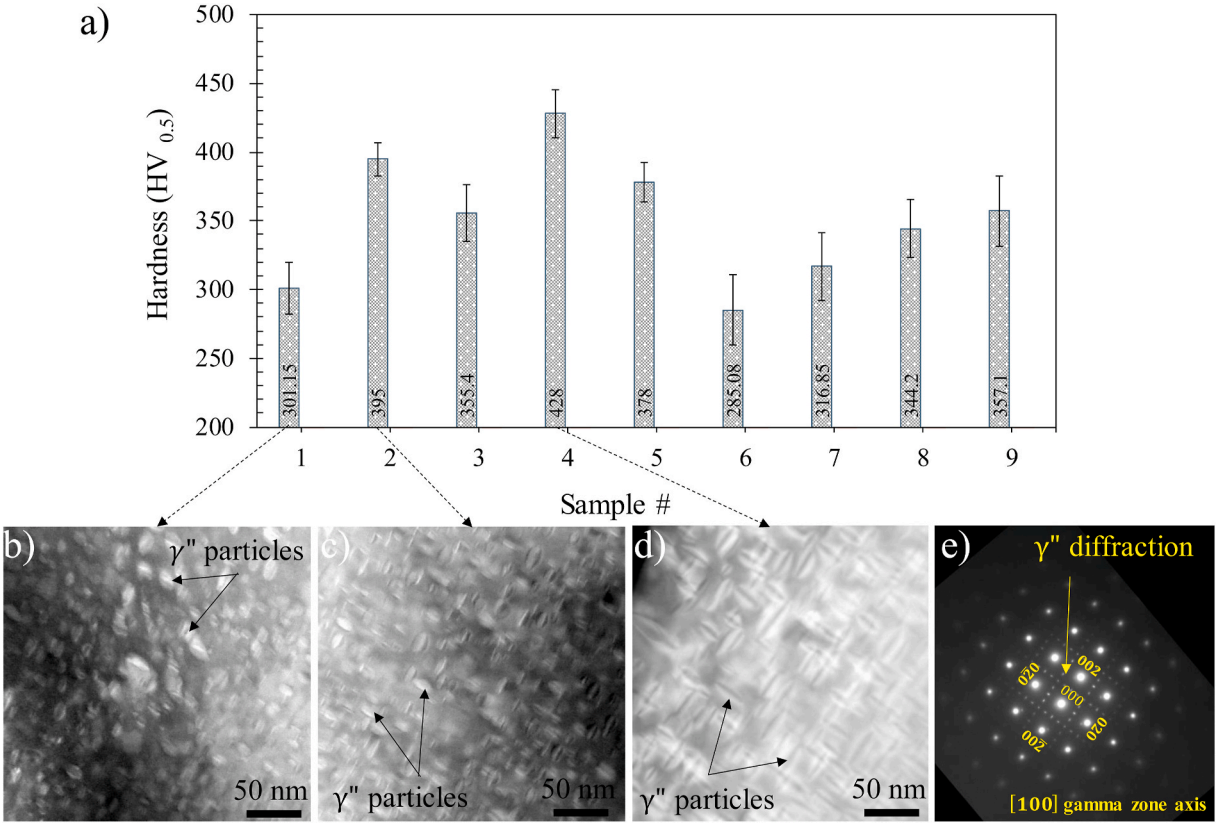

Fig. 10. a) Micro-Vickers hardness of samples manufactured in various conditions, b-d) bright-field and dark-field TEM images from samples #1, #2, and #4, and e) the SAD pattern along the [100] gamma zone axis.

coarsened, leading to a peak hardness value of ~425 $HV_{0.5}$. The size of the γ" precipitates considering that the precipitates had a disc-shaped morphology; the longer side (supposed to be the diameter) and shorter side (supposed to be the thickness) was measured manually from the dark-field (DF) and bright-field (BF) TEM images using the ImageJ software. In addition, the quantitative results achieved by SAXS also showed good agreement with the TEM results. The SAD patterns were used to identify and confirm the γ" precipitates inside the grains by the lattice parameters. An example of the SAD pattern oriented along the [100] zone axis is shown in Fig. 10c. The lattice parameters of the γ" precipitates with the body-centered tetragonal (BCT) structure calculated from the indexing of the SAD patterns are 'a' = 3.61 Å and 'c' = 7.04 Å. The 'a' lattice parameter of the corresponding austenite matrix, with the FCC crystallographic structure, is 3.60 Å, which shows a great agreement with the reported lattice parameters in Refs. [9,23]. The SAXS analysis performed in the same location of each sample showed that the length (radius of gyration) of the γ" precipitates in the fully-columnar, hemispherical melt pools with mixed morphology, and fully-equiaxed grain morphologies were 58 ± 7, 62 ± 5, and 70 ± 2 nm, respectively. Larger size of the γ" precipitates is attributed to the cooling rate, which is higher in the equiaxed grain structure as given in Table 2. In the slower cooling rate, the chance of Nb segregation is higher,

leading to the formation of the Nb-rich phases, such as carbides or δ phase in the expense of the γ" precipitates [28]. From both TEM and SAXS characterization of the γ" precipitates, it was shown that the higher hardness of the sample with the equiaxed grain morphology was due to the coarser γ" precipitates. By increasing the size of the γ" precipitates, the coherency strain increases [60], leading to higher distortions in the matrix, which prohibit dislocation movements.

4. Conclusions

A unique melting strategy was developed to facilitate the columnar-to-equiaxed grain morphology transition in Alloy 718 manufactured via electron beam-powder bed fusion (EB-PBF). The microstructural tailoring is achieved by extensive changes in the thermal gradient direction during solidification. It was found that it is possible to locally alter the grain morphology of a part by controlling the melt pool geometry. The main conclusions emerging from the present study are as follows:

- The EB-PBF-manufactured samples exhibited the columnar-to-equiaxed grain morphology transition using a very wide line offset, slow scanning speed, high line order number and secondary melting of each layer. Four different types of microstructure were achieved and classified based on the grain's morphology, including fully-columnar, fully-equiaxed, hemispherical melt pool with mixed grains, and mixed grain. The main reason for the formation of the four grain morphologies was the reduction in the overlap zone between two adjacent melt pools and also the re-melting depth while adding a new layer, which hindered the epitaxial grain growth by altering the thermal gradient direction significantly. When the overlap between two adjacent melt pools was below 15 %, fully-equiaxed grain morphology was achieved, whereas increasing the overlap to ~20–25 % led to the formation of the hemispherical melt pools with mixed columnar-equiaxed grains. Moreover, when the overlap exceeded 40 %, either columnar or random mixed grain morphology was formed. The typical texture was <001>; however, the texture was reduced through the transition from the columnar-to-equiaxed grain morphology.
- The solidification cracks and long strings of the shrinkage defects were found. The average total crack/shrinkage defects were measured as TSL and TCL in all the samples. The sample with the equiaxed grain morphology showed the lowest level of TSL and TCL. The amount of the cracks and the shrinkage defects was reduced by increasing the scanning speed and line offset. The thermal stress applied to the melt pools during solidification was the main source for the formation of such defects. The width-to-depth ratio of the melt pool and the grain boundary angles were identified as critical factors to the amount TSL and TCL.
- The size of the γ" precipitates increased during the columnar-to-equiaxed grain morphology transition, leading to the highest hardness value in the equiaxed grain morphology. Moreover, high grain boundary density in the equiaxed grain morphology was also resulted in the higher hardness value.

CRediT authorship contribution statement

Paria Karimi: Conceptualization, Methodology, writing, Writing – original draft. **Esmaeil Sadeghi:** Data curation, reviewing of the first draft. **Joakim Ålgårdh:** Reviewing the first draft, Supervision. **Jonas Olsson:** Manufacturing. **Magnus Hörnqvist Colliander:** Data curation, reviewing and editing. **Peter Harlin:** Reviewing and editing. **Ehsan Toyserkani:** Reviewing and editing, Supervision. **Joel Andersson:** Reviewing and editing, Supervision.

Declaration of competing interest

The authors declare that they have no known competing financial interests or personal relationships that could have appeared to influence the work reported in this paper.

Acknowledgments

Funding from the "European Regional Development Fund," the "Simulation and Control of Material affecting Processes" (SiCoMap), and the "Sustainable Manufacturing Through Next-Generation Additive Process" (SUMAN-Next) projects, with funding from the KK foundation, are highly acknowledged. Dr. Carmen Andrei and Mr. Jhoynner Martinez from McMaster University are highly appreciated for their great support with TEM characterization. Mr. Reza Esmaeilizadeh, Ali Keshavarzkermani, and Mr. Henry Ma from Waterloo University also highly appreciated for their valuable input concerning TEM analysis and computed tomography characterization.

References

[1] S. Kou, Welding Metallurgy, second ed., Wiley-Interscience, Hoboken, N.J, 2003.
[2] I. Weld Metal Solidification, Grain Structure," in *Welding Metallurgy*, John Wiley & Sons, Ltd, 2003, pp. 170–198, https://doi.org/10.1002/0471434027.ch7.
[3] E. Sadeghimeresht, et al., Isothermal oxidation behavior of EBM-additive manufactured alloy 718, in: In Proceedings Of the 9th International Symposium On Superalloy 718 & Derivatives: Energy, Aerospace, and Industrial Applications, 2018, pp. 219–240.
[4] E. Sadeghi, P. Karimi, N. Israelsson, J. Shipley, T. Månsson, T. Hansson, Inclusion-induced fatigue crack initiation in powder bed fusion of Alloy 718, Addit. Manuf. 36 (Dec. 2020) 101670, https://doi.org/10.1016/j.addma.2020.101670.
[5] W. Kurz, C. Bezençon, M. Gäumann, Columnar to equiaxed transition in solidification processing, Sci. Technol. Adv. Mater. 2 (1) (Mar. 2001) 185, https://doi.org/10.1016/S1468-6996(01)00047-X.
[6] R.R. Dehoff, et al., Site specific control of crystallographic grain orientation through electron beam additive manufacturing, Mater. Sci. Technol. 31 (8) (Jun. 2015) 931–938, https://doi.org/10.1179/1743284714Y.0000000734.
[7] A. Prasad, et al., Towards understanding grain nucleation under Additive Manufacturing solidification conditions, Acta Mater. 195 (Aug. 2020) 392–403, https://doi.org/10.1016/j.actamat.2020.05.012.
[8] M.M. Kirka, et al., Strategy for texture management in metals additive manufacturing, JOM 69 (3) (Mar. 2017) 523–531, https://doi.org/10.1007/s11837-017-2264-3.
[9] A. Mostafa, I. Picazo Rubio, V. Brailovski, M. Jahazi, M. Medraj, Structure, texture and phases in 3D printed IN718 alloy subjected to homogenization and HIP treatments, Metals 7 (6) (Jun. 2017), https://doi.org/10.3390/met7060196. Art. no. 6.
[10] P. Karimi, Electron Beam Melting of Alloy 718 : Influence of Process Parameters on the Microstructure, Licentiate Thesis, University West, Trollhattan, Sweden, 2018. Accessed: Aug. 06, 2019. [Online]. Available: urn:nbn:se:hv:diva-13140.
[11] P. Karimi, E. Sadeghi, D. Deng, H. Gruber, J. Andersson, P. Nylen, Influence of build layout and orientation on microstructural characteristics of electron beam melted Alloy 718, Int. J. Adv. Manuf. Technol. 99 (S1) (2018) 2903–2913, https://doi.org/10.1007/s00170-018-2621-6.
[12] P. Karimi, E. Sadeghi, J. Ålgårdh, J. Andersson, "EBM-manufactured single tracks of Alloy 718 : influence of energy input and focus offset on geometrical and microstructural characteristics, Mater. Char. 148 (2019) 88–99.
[13] P. Karimi, E. Sadeghi, P. Åkerfeldt, J. Ålgårdh, J. Andersson, Influence of successive thermal cycling on microstructure evolution of EBM-manufactured alloy 718 in track-by-track and layer-by-layer design, Mater. Des. 160 (2018) 427–441, https://doi.org/10.1016/j.matdes.2018.09.038.
[14] F. Ahsan, L. Ladani, Temperature profile, bead geometry, and elemental evaporation in laser powder bed fusion additive manufacturing process, JOM 72 (1) (Jan. 2020) 429–439, https://doi.org/10.1007/s11837-019-03872-3.
[15] F. Ahsan, J. Razmi, L. Ladani, Experimental measurement of thermal diffusivity, conductivity and specific heat capacity of metallic powders at room and high temperatures, Powder Technol. 374 (Sep. 2020) 648–657, https://doi.org/10.1016/j.powtec.2020.07.043.
[16] Additive Manufacturing of Metals," *DEStech Publishing Inc.* https://www.destechpub.com/product/additive-manufacturing-metals/(accessed Jun. 29, 2021).
[17] P. Nandwana, M. Kirka, A. Okello, R. Dehoff, Electron beam melting of Inconel 718: effects of processing and post-processing, Mater. Sci. Technol. 34 (5) (2018) 612–619, https://doi.org/10.1080/02670836.2018.1424379. Mar.
[18] J. Karlsson, M. Norell, U. Ackelid, H. Engqvist, J. Lausmaa, "Surface oxidation behavior of Ti–6Al–4V manufactured by electron beam melting (EBM®), J. Manuf. Process. 17 (1) (2015) 120–126.
[19] R.R. Dehoff, M.M. Kirka, F.A. List, K.A. Unocic, W.J. Sames, Crystallographic texture engineering through novel melt strategies via electron beam melting: inconel 718, Mater. Sci. Technol. 31 (8) (Jun. 2015) 939–944, https://doi.org/10.1179/1743284714Y.0000000697.

[20] C. Körner, H. Helmer, A.B. s, R.F. Singer, Tailoring the Grain Structure of IN718 during Selective Electron Beam Melting, 2014, https://doi.org/10.1051/matecconf/20141408001.
[21] H. Helmer, A. Bauereiß, R.F. Singer, C. Körner, Grain structure evolution in Inconel 718 during selective electron beam melting, Mater. Sci. Eng. Struct. Mater. Prop. Microstruct. Process. 668 (2016) 180–187, https://doi.org/10.1016/j.msea.2016.05.046.
[22] A. Strondl, R. Fischer, G. Frommeyer, A. Schneider, "Investigations of MX and γ′/γ″ precipitates in the nickel-based superalloy 718 produced by electron beam melting, Mater. Sci. Eng., A 480 (1) (May 2008) 138–147, https://doi.org/10.1016/j.msea.2007.07.012.
[23] W.J. Sames V, Additive Manufacturing of Inconel 718 Using Electron Beam Melting: Processing, Post-processing, & Mechanical Properties, 2015. Accessed: May 09, 2019. [Online]. Available: http://adsabs.harvard.edu/abs/2015PhDT.....337S.
[24] P. Karimi, E. Sadeghi, J. Ålgårdh, P. Harlin, J. Andersson, Effect of build location on microstructural characteristics and corrosion behavior of EB-PBF built Alloy 718, Int. J. Adv. Manuf. Technol. 106 (7) (Feb. 2020) 3597–3607, https://doi.org/10.1007/s00170-019-04859-9.
[25] P. Karimi, E. Sadeghi, J. Ålgårdh, C. Kumara, A. Keshavarzkermani, R. Esmaeilizadeh, E. Toyserkani, J. Andersson, Columnar-to-equiaxed grain transition in powder bed fusion via mimicking casting solidification and promoting in-situ recrystallization, Addittive Manufacturing (Oct. 2020).
[26] C.A. Schneider, W.S. Rasband, K.W. Eliceiri, NIH Image to ImageJ: 25 years of image analysis, Nat. Methods 9 (7) (Jul. 2012) 671–675.
[27] F. De Geuser, A. Deschamps, Precipitate characterisation in metallic systems by small-angle X-ray or neutron scattering, Compt. Rendus Phys. 13 (3) (Apr. 2012) 246–256, https://doi.org/10.1016/j.crhy.2011.12.008.
[28] P. Karimi Neghlani, "Electron beam-powder bed fusion of Alloy 718 : effect of process parameters on microstructure evolution, Accessed: Mar. 15, 2021. [Online]. Available: http://urn.kb.se/resolve?urn=urn:nbn:se:hv:diva-16013, , 2020.
[29] Y.L. Hu, et al., Effect of heat treatment on the microstructural evolution and mechanical properties of GH4099 additive-manufactured by directed energy deposition, J. Alloys Compd. 800 (Sep. 2019) 163–173, https://doi.org/10.1016/j.jallcom.2019.05.348.
[30] Y.S. Lee, M.M. Kirka, N. Raghavan, R.R. Dehoff, Simulation of spot melting scan strategy to predict columnar to equiaxed transition in metal additive manufacturing, in: In Proceeding of Solid Free Form Fabrication Symposium, United States of America, Austin, Texas, Aug. 2017, pp. 1005–1017.
[31] A. Hellawell, S. Liu, S.Z. Lu, Dendrite fragmentation and the effects of fluid flow in castings, JOM 49 (3) (Mar. 1997) 18–20, https://doi.org/10.1007/BF02914650.
[32] H.B. Dong, P.D. Lee, "Simulation of the columnar-to-equiaxed transition in directionally solidified Al–Cu alloys, Acta Mater. 53 (3) (Feb. 2005) 659–668, https://doi.org/10.1016/j.actamat.2004.10.019.
[33] P. Karimi, D. Deng, E. Sadeghimeresht, J. Olsson, J. Ålgårdh, J. Andersson, Microstructure development in track-by-track melting of EBM-manufactured alloy 718, in: In Proceedings Of the 9th International Symposium On Superalloy 718 & Derivatives: Energy, Aerospace, and Industrial Applications, Springer, Cham, 2018, pp. 643–654, https://doi.org/10.1007/978-3-319-89480-5_42.
[34] M.M. Kirka, K.A. Unocic, N. Raghavan, F. Medina, R.R. Dehoff, S.S. Babu, Microstructure development in electron beam-melted inconel 718 and associated tensile properties, JOM 68 (3) (Mar. 2016) 1012–1020, https://doi.org/10.1007/s11837-016-1812-6.
[35] Sindo Kou, Welding Metallurgy, second ed., 2002.
[36] G.E. Bean, T.D. McLouth, D.B. Witkin, S.D. Sitzman, P.M. Adams, R.J. Zaldivar, Build orientation effects on texture and mechanical properties of selective laser melting inconel 718, J. Mater. Eng. Perform. 28 (4) (Apr. 2019) 1942–1949, https://doi.org/10.1007/s11665-019-03980-w.
[37] V. Vasava, D. Joshi, Simulation of shrinkage defect-A review, Int. J. Eng. Trends Technol. 4 (6) (2013) 5.
[38] B. Zhang, Y. Li, Q. Bai, Defect formation mechanisms in selective laser melting: a review, Chin. J. Mech. Eng. 30 (3) (May 2017) 515–527, https://doi.org/10.1007/s10033-017-0121-5.
[39] J.A. Cherry, H.M. Davies, S. Mehmood, N.P. Lavery, S.G.R. Brown, J. Sienz, Investigation into the effect of process parameters on microstructural and physical properties of 316L stainless steel parts by selective laser melting, Int. J. Adv. Manuf. Technol. 76 (5) (Feb. 2015) 869–879, https://doi.org/10.1007/s00170-014-6297-2.
[40] A. Mohammad, A.M. Alahmari, M.K. Mohammed, R.K. Renganayagalu, K. Moiduddin, Effect of energy input on microstructure and mechanical properties of titanium aluminide alloy fabricated by the additive manufacturing process of electron beam melting, Materials 10 (2) (Feb. 2017), https://doi.org/10.3390/ma10020211.
[41] P.A. Hooper, Melt pool temperature and cooling rates in laser powder bed fusion, Addit. Manuf. 22 (Aug. 2018) 548–559, https://doi.org/10.1016/j.addma.2018.05.032.
[42] S. Gorsse, C. Hutchinson, M. Gouné, R. Banerjee, Additive manufacturing of metals: a brief review of the characteristic microstructures and properties of steels, Ti-6Al-4V and high-entropy alloys, Sci. Technol. Adv. Mater. 18 (1) (Dec. 2017) 584–610, https://doi.org/10.1080/14686996.2017.1361305.
[43] R.-J. Wang, L. Wang, L. Zhao, Z. Liu, Influence of process parameters on part shrinkage in SLS, Int. J. Adv. Manuf. Technol. 33 (5) (Jun. 2007) 498–504, https://doi.org/10.1007/s00170-006-0490-x.
[44] E. Chauvet, et al., Hot cracking mechanism affecting a non-weldable Ni-based superalloy produced by selective electron Beam Melting, Acta Mater. 142 (Jan. 2018) 82–94, https://doi.org/10.1016/j.actamat.2017.09.047.
[45] S.K. Kim, Y.D. Lee, K. Hansson, H. Fredriksson, Influence of cooling rate on the hot cracking formation of nickel rich alloys, ISIJ Int. 42 (5) (2002) 512–519, https://doi.org/10.2355/isijinternational.42.512.
[46] N. Lu, et al., Hot cracking behavior and mechanism of a third-generation Ni-based single-crystal superalloy during directed energy deposition, Addit. Manuf. 34 (Aug. 2020) 101228, https://doi.org/10.1016/j.addma.2020.101228.
[47] L. Yuan, Solidification defects in additive manufactured materials, JOM 71 (9) (Sep. 2019) 3221–3222, https://doi.org/10.1007/s11837-019-03662-x.
[48] E. Hallberg, Investigation of Hot Cracking in Additive Manufactured Nickel-Base Superalloys, Chalmers Univ. Technol. Depart. Ind. Mater. Sci. (2018) [Online]. Available: https://hdl.handle.net/20.500.12380/255646.
[49] S. Singh, K. Hurtig, J. Andersson, Investigation on effect of welding parameters on solidification cracking of austenitic stainless steel 314, Procedia Manuf. 25 (2018) 351–357, https://doi.org/10.1016/j.promfg.2018.06.103.
[50] M. Ramsperger, R.F. Singer, C. Körner, Microstructure of the nickel-base superalloy CMSX-4 fabricated by selective electron beam melting, Metall. Mater. Trans. 47 (3) (Mar. 2016) 1469–1480, https://doi.org/10.1007/s11661-015-3300-y.
[51] P. Mercelis, J.-P. Kruth, Residual stresses in selective laser sintering and selective laser melting, Rapid Prototyp. J. (Oct. 2006), https://doi.org/10.1108/13552540610707013.
[52] K. Shinozaki, P. Wen, M. Yamamoto, K. Kadoi, Y. Kohno, T. Komori, Effect of grain size on solidification cracking susceptibility of type 347 stainless steel during laser welding, Q. J. Jpn. Weld Soc. 29 (3) (2011) 90s–94s, https://doi.org/10.2207/qjjws.29.90s.
[53] P. Jiang, et al., Fine grains reduce cracking susceptibility during solidification: insights from phase-field simulations, JOM 71 (9) (Sep. 2019) 3223–3229, https://doi.org/10.1007/s11837-019-03342-w.
[54] P. Kontis, et al., Atomic-scale grain boundary engineering to overcome hot-cracking in additively-manufactured superalloys, Acta Mater. 177 (Sep. 2019) 209–221, https://doi.org/10.1016/j.actamat.2019.07.041.
[55] M. Lee, ORCID:0000000249791240) Kirka, J. Ferguson II, and V. (ORCID: 0000000303312598) Paquit, "Correlations of cracking with scan strategy and build geometry in electron beam powder bed additive manufacturing, Addit. Manuf. 32 (Jan. 2020), https://doi.org/10.1016/j.addma.2019.101031.
[56] J.J. Schirra, D. Viens, Metallurgical Factors Influencing the Machinability of Inconel 718 (1994), https://doi.org/10.7449/1994/SUPERALLOYS_1994_827_838.
[57] S. Azadian, "Aspects of Precipitation in Alloy Inconel 718," Doctoral Thesis, Luleå Tekniska Universitet, 2004. Accessed: May 09, 2019. [Online]. Available: http://muep.mau.se/handle/2043/4919.
[58] J. Andersson, "Weldability of Precipitation Hardening Superalloys – Influence of Microstructure," Doctoral Thesis, Chalmers University, 2011.
[59] John K. Tien, Superalloys, Supercomposites and Superceramics, first ed., 1989. Accessed: Aug. 13, 2019. [Online]. Available: https://www.elsevier.com/books/superalloys-supercomposites-and-superceramics/tien/978-0-12-690845-9.
[60] A. Devaux, et al., Gamma double prime precipitation kinetic in Alloy 718, Mater. Sci. Eng., A 486 (1) (Jul. 2008) 117–122, https://doi.org/10.1016/j.msea.2007.08.046.